Research Square

Preprints are preliminary reports that have not undergone peer review.
They should not be considered conclusive, used to inform clinical practice,
or referenced by the media as validated information.

Integrated artificial photosynthesis and microbial bioprocessing systems for solar biofuel and bioproduct production

Devesh Ojha

dojha@lko.amity.edu

Amity University

Bandana Ojha

Amity University

Research Article

Keywords: artificial photosynthesis, biohybrid systems, microbial electrosynthesis, solar-to-chemical efficiency, techno-economic analysis, life cycle assessment, polyhydroxybutyrate, process control

Posted Date: November 9th, 2026

DOI: https://doi.org/10.21203/rs.3.rs-11392066/v1

License: This work is licensed under a Creative Commons Attribution 4.0 International License.
Read Full License

Additional Declarations: No competing interests reported.

Integrated artificial photosynthesis and microbial bioprocessing systems for solar biofuel and bioproduct production

Devesh Ojha[a,*], Bandana Ojha [b]

[a] Department of Civil Engineering, Amity University, Lucknow, India;

[b] Department of Computer Science & Engineering, Amity University, Ranchi, India

[*] Corresponding author: Devesh Ojha
Department of Civil Engineering Amity University, Lucknow, India
E-mail: dojha@lko.amity.edu
ORCID: 0000-0003-2814-9555

Highlights

- Three biohybrid architectures compared within one quantitative framework
- Efficiency cascade bounds solar-to-chemical yield at 4–11% under stated assumptions
- Substrate inhibition creates an unstable branch that requires closed-loop control
- Anti-windup PI control cut peak formate excursion from 207 to 48 mM in simulation
- Biogenic carbon credit dominates the apparent climate benefit of PHB routes

Abstract

Coupling abiotic solar capture with microbial biosynthesis integrated artificial photosynthesis–microbial bioprocessing (IAP-MB) could convert sunlight, water and CO_2 into fuels and polymers at areal efficiencies well above those of crops, which typically remain below 1%. Here we critically review three architectures decoupled photovoltaic–electrolysis/fermentation (A), electrode-attached biofilms (B) and photosensitised cells (C) and combine the literature with transparent screening calculations. A cascade analysis bounds the solar-to-chemical efficiency of Architecture A at 4.0–10.9% (base case 7.2%) and identifies electrolysis and bioconversion as the main leverage points. Substrate-inhibited uptake kinetics (Andrews model) imply an unstable operating branch above the optimum carrier concentration (9.8 mM for the constants used), so unmanaged supply–demand mismatch causes runaway accumulation; in simulation, a PI controller with back-calculation anti-windup reduced the peak formate concentration from 207 to 48 mM relative to an unprotected PI loop. Using the authors' preliminary plant model (10,000 t PHB yr^{-1}), recomputed levelised costs are US$2.19 kg^{-1} (A) and US$3.23 kg^{-1} (B), dominated by discount rate and operating cost, and photoelectrode lifetimes near one year add roughly US$0.8 kg^{-1} to B. Stoichiometrically consistent life-cycle accounting shows that the climate benefit of PHB routes hinges on the biogenic carbon credit (2.04 kg CO_2 per kg PHB): burdens alone are 1.80 (A) and 3.10 (B) kg CO_2-eq kg^{-1}, versus 1.98 for polypropylene. A research roadmap and reporting recommendations close to the paper.

Keywords: artificial photosynthesis; biohybrid systems; microbial electrosynthesis; solar-to-chemical efficiency; techno-economic analysis; life cycle assessment; polyhydroxybutyrate; process control

1. Introduction

Replacing fossil carbon in fuel and materials supply chains requires conversion pathways that are both low-carbon and land-frugal. Terrestrial biofuels have struggled on both counts: land clearing creates a carbon debt that can take decades to repay (Fargione et al., 2008; Searchinger et al., 2008), and the underlying biophysics is unfavourable. The theoretical maximum efficiency of converting sunlight into biomass is about 4.6% for C_3 and 6% for C_4 photosynthesis under ambient CO_2 (Zhu et al., 2008), and realised annual efficiencies of crops are far lower, generally below 1% (Zhu et al., 2010; Blankenship et al., 2011).

Artificial photosynthesis offers a way around the biological light-harvesting bottleneck (Lewis and Nocera, 2006; Kim et al., 2015). Photovoltaic (PV)–electrolysis and photoelectrochemical (PEC) devices already reach solar-to-hydrogen efficiencies of 19% for a monolithic PEC device (Cheng et al., 2018) and above 30% for concentrated III–V PV coupled to electrolysis (Jia et al., 2016), and recent assessments argue that engineered systems can greatly exceed natural photosynthesis (Dogutan and Nocera, 2019). Their drawback is the product slate: hydrogen, CO, formate and acetate are simple molecules, whereas fuels, polymers and foods are complex. Microorganisms are excellent at precisely that second step. Integrated artificial photosynthesis–microbial bioprocessing (IAP-MB) therefore merges abiotic solar capture with microbial carbon fixation and biosynthesis, as first demonstrated for isopropanol (Torella et al., 2015), higher alcohols (Li et al., 2012) and biomass/fuels (Liu et al., 2016). The three architectures are summarised in Figure 1, and Figure 2 compares reported and theoretical conversion efficiencies relevant to IAP-MB; the bars refer to different bases and should be read accordingly.

Recent reviews have catalogued materials, microbes and interfaces (Fang et al., 2020; Cestellos-Blanco et al., 2020; Kornienko et al., 2018), photosynthetic bioprocess engineering (Stephens et al., 2021) and integrated biopolymer–bioenergy systems (Pagliano et al., 2017). What is still missing is a single quantitative frame that links (i) architecture-specific efficiency limits, (ii) metabolic and kinetic constraints on electron delivery, (iii) abiotic–biotic interfacial failure modes, (iv) reactor and control engineering, and (v) techno-economic and life-cycle consequences. This paper contributes such a frame. Specifically, we (1) classify IAP-MB architectures and tabulate representative performance using only values reported in primary studies; (2) derive an efficiency cascade and a kinetic stability argument that explain why supply–demand matching is central; (3) re-evaluate an integrated preliminary plant model for polyhydroxybutyrate (PHB) production at 10,000 t yr^{-1}, including reactor sizing, feedback control, techno-economics and life-cycle accounting; and (4) propose a prioritised roadmap with measurable targets.

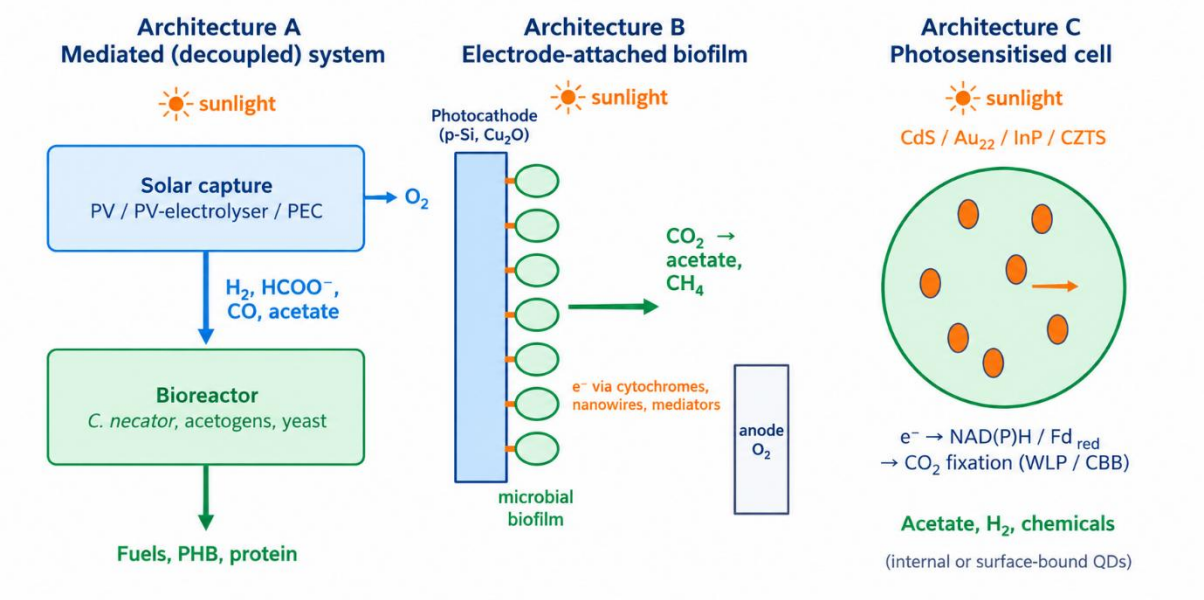


Figure 1. Conceptual overview of the three IAP-MB architectures. (A) Decoupled: a solar-driven electrolyser generates soluble carriers (H_2, formate, CO, acetate) that are fed to a separate bioreactor. (B) Electrode-attached: microbes colonise a photocathode and take up electrons directly. (C) Photosensitised cells: semiconductor nanoparticles or clusters on or inside cells supply photoexcited electrons to cellular redox carriers.

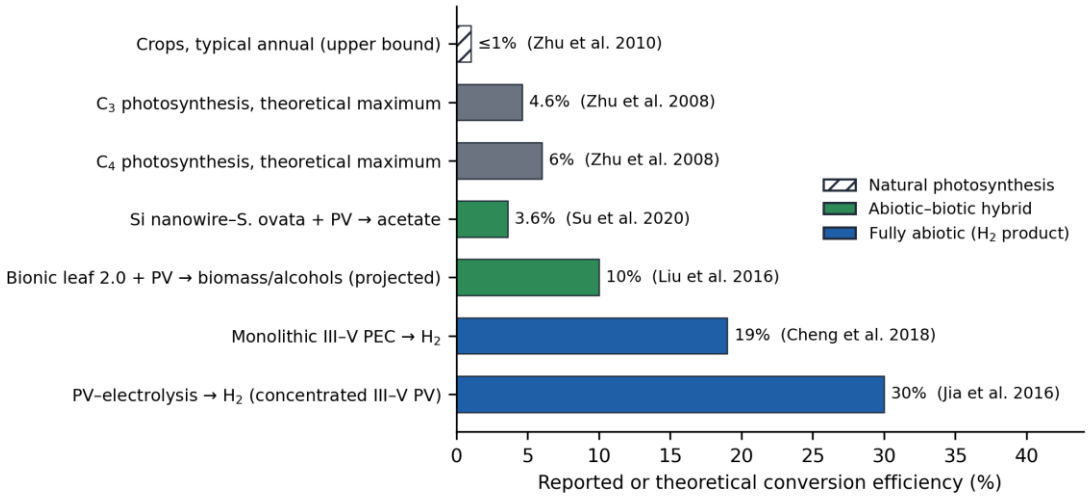


Figure 2. Reported and theoretical conversion efficiencies relevant to IAP-MB. Bars are not directly interchangeable: they refer to biomass or acetate formation (green, grey) or to hydrogen (blue), and the bionic-leaf value is a projection for PV-coupled operation. Sources: (Zhu et al., 2010); (Zhu et al., 2008); (Su et al., 2020); (Liu et al., 2016); (Cheng et al., 2018); (Jia et al., 2016).

2. Scope and approach

This is a critical, narrative review supplemented by screening-level calculations. A structured literature search was conducted using Scopus, Web of Science, and ScienceDirect, with supplementary searches of Google Scholar used to identify relevant studies that may not have

been captured in the primary databases. Priority was given to landmark and highly cited studies, to recent work published up to 2026, and to papers that report quantitative metrics on a well-defined basis. Numerical values attributed to a source are those given by the source; where a study does not report a metric on a solar-to-chemical basis, we say so rather than infer one.

Sections 6–9 contain the authors' own calculations. They use (i) literature-anchored assumptions for the efficiency cascade (Section 6), and (ii) a preliminary plant, reactor and inventory model (Sections 7–9) whose inputs are listed in the tables and are treated as design assumptions pending experimental validation. No new experimental data are reported, and the genome-scale analysis in Section 4.3 is presented as a methodological framework rather than as results. All calculations are reproducible from the stated inputs.

3. Integrated biohybrid architectures

3.1 Classification

We distinguish three architectures by where light is absorbed and how electrons reach the cell (Figure 1). In Architecture A (decoupled PV–electrolysis/fermentation), solar electricity drives CO_2 or water electrolysis, and soluble carriers are transferred to a separate bioreactor in which light is not required. In Architecture B (electrode-attached biofilm), microorganisms colonise a conductive (photo)electrode and accept electrons via outer-membrane cytochromes, conductive appendages or diffusible mediators. In Architecture C (photosensitised cell), semiconductor nanoparticles or metal clusters precipitated on the cell surface or formed inside the cell absorb light and inject photoexcited electrons into the cell's redox carriers. Architecture B is often described by analogy with direct interspecies electron transfer, in which electrons move directly between cells (Lovley, 2017); here the partner is an electrode rather than a second organism.

3.2 Architecture A: decoupled electrolysis and fermentation

The strongest quantitative evidence so far exists for A. Liu et al. (2016) coupled water-splitting catalysts to engineered *Cupriavidus necator*, reporting CO_2-reduction energy efficiencies of about 50% from electricity and about 10% projected for PV-coupled operation. Torella et al. (2015) and Li et al. (2012) showed biosynthesis of isopropanol and higher alcohols from H_2 and from electrochemically produced formate, respectively. Haas et al. (2018) proposed "technical photosynthesis", in which CO_2 electrolysis is followed by fermentation to longer-chain alcohols, an approach aligned with commercial gas-fermentation experience (Liew et al., 2016). More recently, Hann et al. (2022) coupled CO_2-to-acetate electrolysis to food-producing organisms, reporting about a fourfold higher solar-to-food energetic efficiency than photosynthesis, and Zheng et al. (2022) converted CO_2-derived acetate into glucose and fatty acids using yeast.

The advantages of A are modularity (each stage can be optimised independently), isolation of the cells from photogenerated oxidants and harsh electrode chemistry, and compatibility with high-cell-density fermentation. Its costs are an additional unit operation and the need to manage carrier transfer, buffering and, for formate or H_2, the mass-transfer and toxicity constraints discussed in Sections 4–7. Formate is attractive because it is a soluble, energy-dense carrier

that supports microbial growth and, in engineered *Escherichia coli*, full autotrophy (Gleizer et al., 2019; Yishai et al., 2016); a quantitative comparison of carriers is given by Claassens et al. (2019) and Claassens et al. (2018). Techno-economic studies of CO_2 electrolysis emphasise electricity price, energy efficiency and current density as the decisive factors (Jouny et al., 2018; De Luna et al., 2019).

3.3 Architecture B: electrode-attached biofilms

In B, acetogens such as *Sporomusa ovata* colonise silicon nanowire or other photocathodes and reduce CO_2 to acetate using electrons from the electrode (Nichols et al., 2015; Liu et al., 2015). Su et al. (2020) reported close-packed nanowire–bacteria hybrids reaching about 3.6% solar-to-chemical efficiency for acetate with PV assistance, and Rishan et al. (2026) coupled a Cu_2ZnSnS_4 photocathode–*S. ovata* hybrid to *Clostridium kluyveri* fermentation to reach C4–C6 fatty acids. Microbial electrosynthesis in the dark provided the conceptual basis (Rabaey and Rozendal, 2010; Nevin et al., 2010), and critical assessments warn that rates, scale and energy efficiency remain limiting (Prévoteau et al., 2020). Mechanistic understanding of electron uptake via outer-membrane cytochromes, conductive nanostructures and redox mediators is advancing (Shi et al., 2016; Logan et al., 2019; Kracke et al., 2015), but the electrode area needed to supply a bioreactor-scale electron flux, the stability of photocathodes in culture medium and biofouling remain open problems.

3.4 Architecture C: photosensitised cells

Sakimoto et al. (2016) showed that *Moorella thermoacetica* can self-photosensitise by precipitating CdS nanoparticles, enabling light-driven CO_2-to-acetate conversion. Ultrafast spectroscopy has since resolved electron-transfer dynamics at this interface (Kornienko et al., 2016), and cells that form intracellular gold nanoclusters can also be photosensitised (Zhang et al., 2018). The concept extends beyond acetogens: CdS-decorated yeast produced shikimic acid under light (Guo et al., 2018), quantum-dot-modified *E. coli* supported light-driven biochemical synthesis (Ding et al., 2019), and CdS-decorated *E. coli* showed enhanced H_2 production (Wang et al., 2017). Acetogens can also use light-driven electrons as an energy source for autotrophic growth (Jin et al., 2021), and a semi-artificial photosynthetic biofilm has been engineered for robust CO_2-to-methane conversion (Chen et al., 2026). A perspective on the physical biology of the material–microbe interface (Sakimoto et al., 2018) emphasises that membrane transport, material toxicity and light stability set the practical limits of C. Quantum yields are frequently reported for C, but solar-to-chemical efficiencies on an incident-sunlight basis are rarely given, which complicates comparison with A and B.

3.5 Comparative assessment

Table 1 summarises representative studies and Table 2 compares the architectures qualitatively. We deliberately avoid assigning single “maximum efficiency” or volumetric-yield ranges per architecture, because published studies report different metrics (quantum yield, Faradaic efficiency, energy efficiency, solar-to-chemical efficiency) on different bases and with different light, bias and electrode areas; any single range would imply a comparability that the literature does not support.

Table 1. Representative IAP-MB studies and the metrics reported by the original authors.

Study	Arch.	Solar capture / electron source	Microorganism	Product(s)	Key reported finding
Li et al. (2012)	A	Electrochemical formate	*C. necator* (engineered)	Isobutanol, 3-methyl-1-butanol	Integrated electromicrobial conversion of CO_2 to higher alcohols
Torella et al. (2015)	A	Co–P / NiMoZn water-splitting catalysts (H_2)	*C. necator* (engineered)	Isopropanol, biomass	Hybrid microbial–water-splitting system for solar-to-fuels
Liu et al. (2016)	A	Water-splitting catalysts (H_2)	*C. necator*	Biomass, alcohols	≈50% electricity-to-CO_2-reduction efficiency; ≈10% projected with PV
Haas et al. (2018)	A	CO_2 electrolysis	Fermenting anaerobes	Longer-chain alcohols	Technical-photosynthesis route combining electrolysis and fermentation
Hann et al. (2022)	A	CO_2-to-acetate electrolysis	Algae, yeast, plants, fungi	Food biomass	≈4-fold higher solar-to-food efficiency than photosynthesis
Zheng et al. (2022)	A	CO_2-to-acetate electrolysis	Yeast	Glucose, fatty acids	CO_2 upcycled to energy-rich long-chain compounds
Nichols et al. (2015)	B	Si nanowire / TiO_2 photocathode	*S. ovata*	Acetate	Hybrid bioinorganic solar-to-chemical conversion
Su et al. (2020)	B	Close-packed Si nanowires (with PV)	*S. ovata*	Acetate	≈3.6% solar-to-chemical efficiency
Rishan et al. (2026)	B	Cu_2ZnSnS_4 photocathode	*S. ovata* + *C. kluyveri*	C4–C6 fatty acids	Photobiohybrid coupled to chain-elongating fermentation
Sakimoto et al. (2016)	C	Biogenic CdS nanoparticles	*M. thermoacetica*	Acetate	Self-photosensitisation of a non-photosynthetic bacterium
Zhang et al. (2018)	C	Intracellular Au nanoclusters	*M. thermoacetica*	Acetate	Intracellular photosensitisation for solar fuel production
Guo et al. (2018)	C	CdS nanoparticles on cells	*S. cerevisiae*	Shikimic acid	Light-driven fine-chemical production in yeast biohybrids
Wang et al. (2017)	C	CdS nanoparticles on cells	*E. coli*	H_2	Enhanced biological H_2 production
Chen et al. (2026)	B/C	Semiconductor–biofilm interface	Methanogenic biofilm	CH_4	Robust, high-efficiency CO_2-to-methane conversion

Entries are paraphrased from the cited studies; "Arch." follows the classification in Section 3.1. Quantitative values are given only where the source reports them.

Table 2. Qualitative comparison of IAP-MB architectures (authors' synthesis of the cited literature).

Attribute	A: Decoupled PV–EC/fermentation	B: Electrode-attached biofilm	C: Photosensitised cell
Light absorber	Commercial PV or PEC device; separate from cells	Photocathode in contact with biofilm	Nanoparticles or clusters on/in cells

Electron carrier	H_2, formate, CO, acetate (diffusible)	Direct transfer via cytochromes, nanostructures or mediators	Photoexcited electrons to NAD(P)H / ferredoxin
Typical chassis	*C. necator*, acetogens, yeast, algae	*S. ovata*, other electroactive microbes, methanogens	*M. thermoacetica*, *E. coli*, yeast
Best-documented efficiency	≈10% (projected, (Liu et al., 2016)); abiotic stage up to 30% as H_2 (Jia et al., 2016)	≈3.6% solar-to-acetate (Su et al., 2020)	Mostly quantum yield; STC efficiency rarely reported
Exposure of cells to oxidants / photocorrosion products	Low (physical separation)	Moderate (local pH, ROS at electrode)	High (material toxicity, intracellular ROS)
Light requirement of the cell culture	None (dark fermentation)	Light must reach photocathode through medium	Light must penetrate dense suspension
Evidence at larger scale	Gas fermentation is commercial (Liew et al., 2016); integrated systems at bench/pilot	Laboratory scale	Laboratory scale
Main bottleneck	Carrier supply–demand matching; electrolyser and gas–liquid mass transfer	Photocathode lifetime; electron-uptake area and rate	Toxicity; light penetration; recovery of nanomaterials

4. Metabolic and kinetic foundations

4.1 Carbon fixation and energy conservation

Microbial CO_2 fixation in IAP-MB relies mainly on the Wood–Ljungdahl pathway (WLP) in acetogens and on the Calvin–Benson–Bassham (CBB) cycle in hydrogen- and formate-oxidising bacteria such as *C. necator*, a well-characterised producer of polyhydroxyalkanoates (Reinecke and Steinbüchel, 2009). The WLP reduces CO_2 along a methyl branch (via formate and tetrahydrofolate intermediates) and a carbonyl branch (via carbon monoxide dehydrogenase) and combines both at acetyl-CoA synthase (Figure 3). It is energetically frugal, but acetogens operate close to the thermodynamic limit of life and conserve energy through ion-gradient-driven mechanisms rather than substrate-level phosphorylation alone (Ragsdale and Pierce, 2008; Schuchmann and Müller, 2014). Design studies of synthetic carbon-fixation routes show that pathway choice shapes the ATP and reductant cost per fixed carbon (Bar-Even et al., 2010; Schwander et al., 2016), which in turn determines how much of the supplied electron flux can be converted into product.

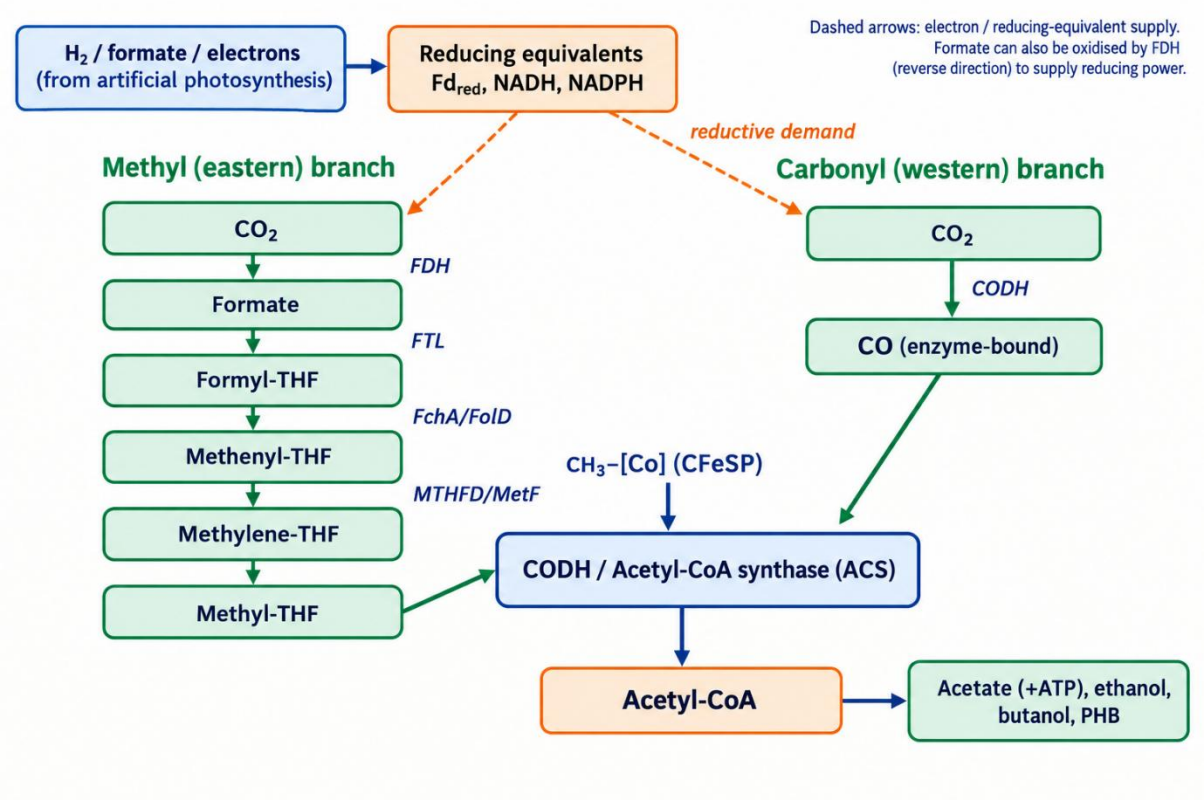


Figure 3. The Wood–Ljungdahl pathway and its coupling to reducing equivalents from artificial photosynthesis. Abbreviations: FDH, formate dehydrogenase; FTL, formate–THF ligase; FchA/FolD, methenyl-THF cyclohydrolase/methylene-THF dehydrogenase; MTHFD/MetF, methylene-THF dehydrogenase/reductase; CODH, carbon monoxide dehydrogenase; ACS, acetyl-CoA synthase; CFeSP, corrinoid iron–sulfur protein; THF, tetrahydrofolate.

4.2 Uptake kinetics and the supply–demand mismatch

When a soluble carrier such as formate or H_2 is fed to a culture, specific uptake is non-monotonic if high concentrations are inhibited. The Andrews (Haldane) form (Andrews, 1968) gives

$$q_S = \frac{q_{max} S}{K_S + S + \frac{S^2}{K_I}} \tag{1}$$

where q_S is the specific uptake rate, q_{max} the maximum uptake rate, S the carrier concentration, K_S the affinity constant and K_I the inhibition constant. Uptake peaks at

$$S_{opt} = \sqrt{K_S K_I} \tag{2}$$

and declines beyond S_{opt}. For K_S = 0.8 mM and K_I = 120 mM (the values used in Section 7.3), S_{opt} = 9.8 mM. Figure 4 shows why these matters. If the carrier is supplied at a flux J, steady states exist where J equals $q_S X$. Below the peak flux there are two: a stable one on the ascending branch and an unstable one on the descending branch, where any positive perturbation in S reduces uptake and drives further accumulation. If J exceeds the peak flux, no steady state exists and S accumulates until limited by the feed concentration or by toxicity, for example through disruption of the proton-motive force by weak acids such as formate. Because artificial

photosynthesis delivers electrons at rates set by sunlight, rather than by cellular demand, this supply–demand mismatch is intrinsic to A, and, in different guise, to B and C.

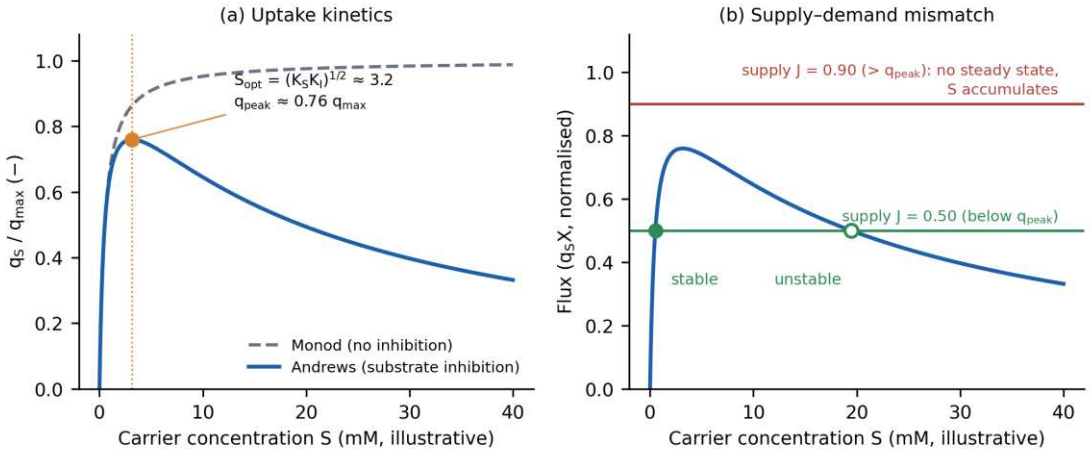


Figure 4. Substrate-inhibited uptake and the supply–demand mismatch. (a) Monod versus Andrews kinetics (K_S = 0.5 mM, K_I = 20 mM, illustrative). (b) Steady states for a constant supply flux J: two for J below the peak (filled, stable; open, unstable) and none for J above the peak flux.

4.3 Genome-scale flux analysis as a design tool

Flux balance analysis (FBA) provides the natural tool for asking how much product can be made per unit of electron input (Orth et al., 2010). Curated genome-scale models exist for model heterotrophs such as *E. coli* (Monk et al., 2017) and for acetogens such as *Clostridium ljungdahlii* (Nagarajan et al., 2013). A practical IAP-MB workflow would (i) constrain the model with the measured carrier uptake flux (H_2, formate or electrode current), (ii) fix growth-associated and non-growth-associated maintenance from chemostat data, (iii) maximise product formation under redox-balance constraints, and (iv) scan the carrier flux to identify where the optimum shifts from product to by-products such as acetate or formate overflow. Linking such a model to the interfacial circuit in Section 5.1 would allow energy losses to be allocated between the abiotic interface, electron uptake and metabolism. We have not performed this analysis here and make no quantitative claims from it.

5. Mechanistic bottlenecks

5.1 Interfacial electron transfer

Electrons must cross at least two interfaces before reaching metabolism: the semiconductor or catalyst surface, and the bio-abiotic boundary where cytochromes, conductive nanostructures or mediators accept charge (Shi et al., 2016; Logan et al., 2019). Figure 5 sketches an equivalent-circuit view in which the solution resistance R_s, charge-transfer resistance R_{ct} and double-layer capacitance C_{dl} describe the abiotic interface; R_{EET} and C_{bio} describe extracellular electron transfer; a Warburg-type element Z_W represents diffusion in the biofilm or boundary layer; and the metabolic sink is the cell's demand for reducing equivalents. Electrochemical impedance and voltammetry can in principle assign the measured losses to these elements, and the physical-biology perspective of Sakimoto et al. (2018) and the spectroscopy of Kornienko

et al. (2016) provide complementary routes to the time scales involved. Because respiratory electron transport is tightly coupled with energy conservation (Kracke et al., 2015), the electron-uptake rate that an electrode or nanoparticle can sustain is bound by the cell's capacity to dissipate it, which is why interfacial kinetics and metabolic demand cannot be optimised separately. This circuit is a conceptual framework; parameter values must be determined experimentally for each system.

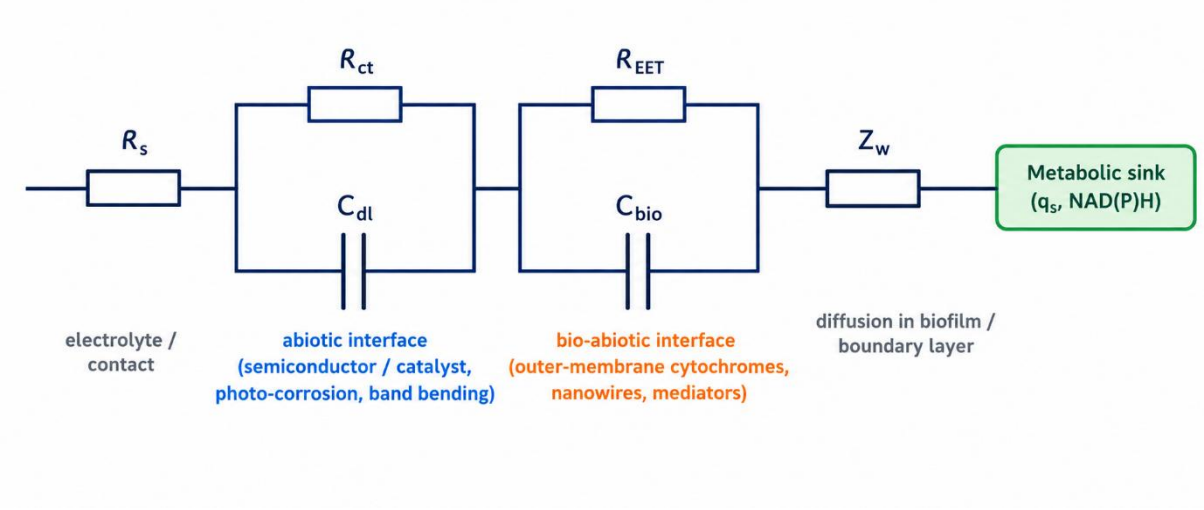


Figure 5. Conceptual equivalent circuit for charge transfer from a solar absorber to the metabolic sink. R_s, solution resistance; R_{ct}/C_{dl}, abiotic charge-transfer resistance and double-layer capacitance; R_{EET}/C_{bio}, extracellular electron-transfer resistance and capacitance; Z_W, mass-transport impedance.

5.2 Reactive oxygen species and material toxicity

Photoexcited carriers, electrode reactions and cellular respiration all generate superoxide, hydrogen peroxide and hydroxyl radicals, which damage iron–sulfur enzymes, membranes and DNA unless detoxified by superoxide dismutase, catalases and peroxidases (Imlay, 2008; Imlay, 2013). In photosensitised cells, the nanomaterial itself is a hazard: cadmium-based nanoparticles are toxic to *E. coli* (Hossain and Mukherjee, 2013), and the cytotoxicity of cadmium-containing quantum dots is linked to Cd^{2+} release, which can be reduced by shell coatings (Derfus et al., 2004). Reviews of photosynthetic bioprocess engineering also identify oxidative stress as a principal constraint (Stephens et al., 2021). Mitigation options therefore include overexpression of catalase and superoxide dismutase, biogenic or capped nanomaterials, and spatial separation of oxidising and reducing reactions as in A.

5.3 Photocorrosion and electrode stability

Many semiconductors are thermodynamically unstable in aqueous media because their own oxidation or reduction potentials lie within the band gap relative to the water redox couples (Chen and Wang, 2012). Atomic-layer-deposited amorphous TiO_2 coatings have been shown to stabilise Si, GaAs and GaP photoanodes over extended operation (Hu et al., 2014), and similar protection strategies are required for photocathodes in culture medium, where biofouling and local pH gradients add to degradation. Electrode lifetime is a direct cost driver for B (Section 8).

5.4 Redox cofactor and flux imbalance

High-rate delivery of reduced carriers can saturate the cell's redox pools, raising NADH/NAD^+ and NADPH/$NADP^+$ ratios, slowing the enzymes that oxidise the carrier (for example formate dehydrogenase) and diverting carbon towards overflow products such as acetate rather than the desired fuel or polymer. In acetogens, reduced ferredoxin and NADH are produced by electron-bifurcating and ion-gradient-coupled enzymes whose operation is constrained by thermodynamics (Schuchmann and Müller, 2014), and in bio electrochemical systems the interplay between electron uptake and energy conservation sets how much current can be converted productively (Kracke et al., 2015). These effects motivate the dynamic control strategy in Section 7.3. Table 3 summarises the principal bottlenecks discussed in this section, together with gas–liquid mass transfer and shear (Section 7), their mechanisms, candidate mitigation strategies and key references.

Table 3. Principal bottlenecks, mechanisms and candidate mitigation strategies.

Bottleneck	Mechanism	Mitigation strategies	Key references
Interfacial electron transfer	Resistance and non-radiative loss at semiconductor–cell interface; limited conductive contacts	Conductive, biocompatible interface layers (e.g., PEDOT: PSS derivatives); nanostructured high-area electrodes; promoting conductive appendages	(Shi et al., 2016; Logan et al., 2019; Su et al., 2020)
ROS and oxidative stress	Superoxide, H_2O_2, •OH from electrodes, photoexcited carriers and respiration	Catalase / SOD overexpression; physical separation of oxidation (A); redox-buffering media	(Imlay, 2008; Imlay, 2013; Stephens et al., 2021)
Nanomaterial toxicity	Cd^{2+} release and membrane damage from CdS/CdSe	Shell coatings; biogenic synthesis; alternative non-toxic absorbers (e.g., Cu_2ZnSnS_4)	(Derfus et al., 2004; Hossain and Mukherjee, 2013; Rishan et al., 2026)
Photocorrosion	Self-oxidation/reduction of semiconductors in water	Protective oxide coatings; band-edge selection	(Chen and Wang, 2012; Hu et al., 2014)
Redox / carrier imbalance	Supply exceeds uptake capacity; substrate inhibition; overflow metabolism	Closed-loop feed control; strain engineering for carrier tolerance	(Andrews, 1968; Gleizer et al., 2019; Schuchmann and Müller, 2014)
Gas–liquid mass transfer and shear	Low solubility of H_2, O_2, CO_2; shear damage at high power input	Gas-lift reactors with staged trays; validated k_La and shear limits	(Garcia-Ochoa and Gomez, 2009; Chisti and Moo-Young, 1987; van 't Riet, 1979)

6. Efficiency cascade

The solar-to-chemical efficiency is defined on an incident-sunlight and product-combustion-enthalpy basis:

$$\eta_{STC} = \frac{R_P \cdot \Delta H_{c,P}}{G \cdot A} \tag{3}$$

where R_P is the product formation rate (kg s^{-1}), $\Delta H_{c,P}$ its energy content, G the incident irradiance and A the collector area. For Architecture A the efficiency factorises into the PV, electrolysis and bioconversion stages:

$$\eta_{STC} = \eta_{PV} \cdot \eta_{EC} \cdot \eta_{bio} \quad (4)$$

Table 4 lists three screening scenarios; the values are assumptions chosen to span the plausible range, not measurements. The conservative, base and optimistic cases yield η_{STC} of 4.0%, 7.2% and 10.9% (Figure 6). The base case is about seven times a 1% crop baseline and exceeds the C_3 theoretical maximum of 4.6% (Zhu et al., 2008), whereas the conservative case falls just below it. The result is consistent in magnitude with the ≈10% projected for PV-coupled operation of the bionic leaf (Liu et al., 2016), which, however, is expressed on a different basis (energy efficiency of CO_2 reduction). Two conclusions follow. First, the product $\eta_{EC} \cdot \eta_{bio}$ must reach roughly 30% for η_{STC} to exceed 7% with a 24%-efficient PV stage. Second, because the three efficiencies multiply, a 10-percentage-point gain in the electrolysis or bioconversion stage is worth as much, in relative terms, as a comparable relative gain in PV efficiency, but is currently far less mature.

Table 4. Efficiency-cascade scenarios for Architecture A (assumptions, not measurements).

Scenario	η_{PV}	η_{EC} (electricity to carrier)	η_{bio} (carrier to product)	η_{STC} (computed)
Conservative	20%	50%	40%	4.0%
Base case	24%	60%	50%	7.2%
Optimistic	26%	70%	60%	10.9%

Energy basis: product combustion enthalpy relative to incident sunlight. η_{EC} and η_{bio} are lumped energy efficiencies; Faradaic and carbon-utilisation efficiencies are subsumed within them.

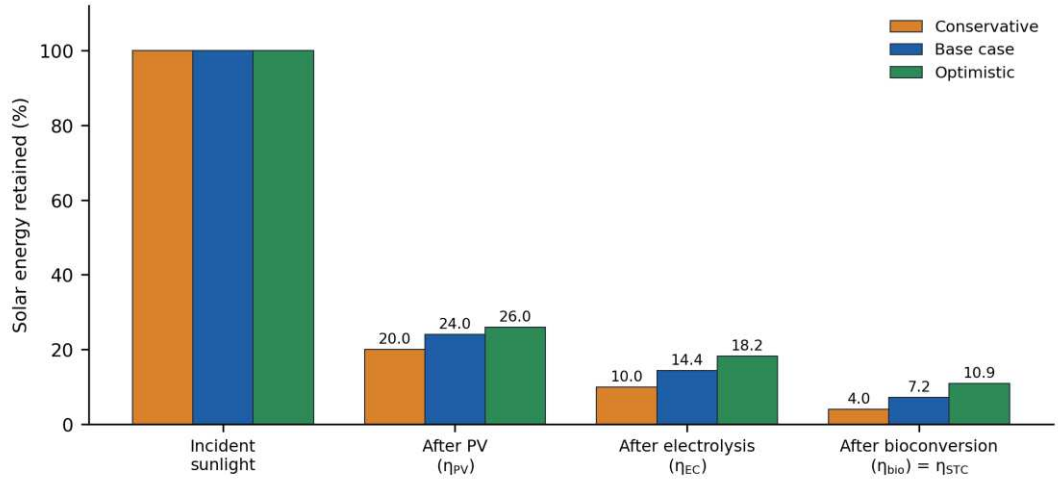


Figure 6. Solar-energy retention along the PV–electrolysis–bioconversion cascade for three scenarios. Values above bars are percentages of incident solar energy remaining after each stage.

7. Process engineering and control of Architecture A

7.1 Process configuration

Figure 7 shows the process considered in the remainder of the paper: a PV field powers a CO_2/H_2O electrolyser producing formate, CO, acetate or H_2; a buffer tank decouples the intermittent solar supply from the continuous bioreactor; and a supervisory controller adjusts

electrolyser current and feed flow using sensor signals. Integrated designs that co-produce several products or valorise residual biomass improve resource use (Pagliano et al., 2017; Novak et al., 2024). For the analysis below, the target product is PHB at 10,000 t yr^{-1}, produced by *C. necator* in continuous dark fermentation on formate; the same layout accommodates biobutanol.

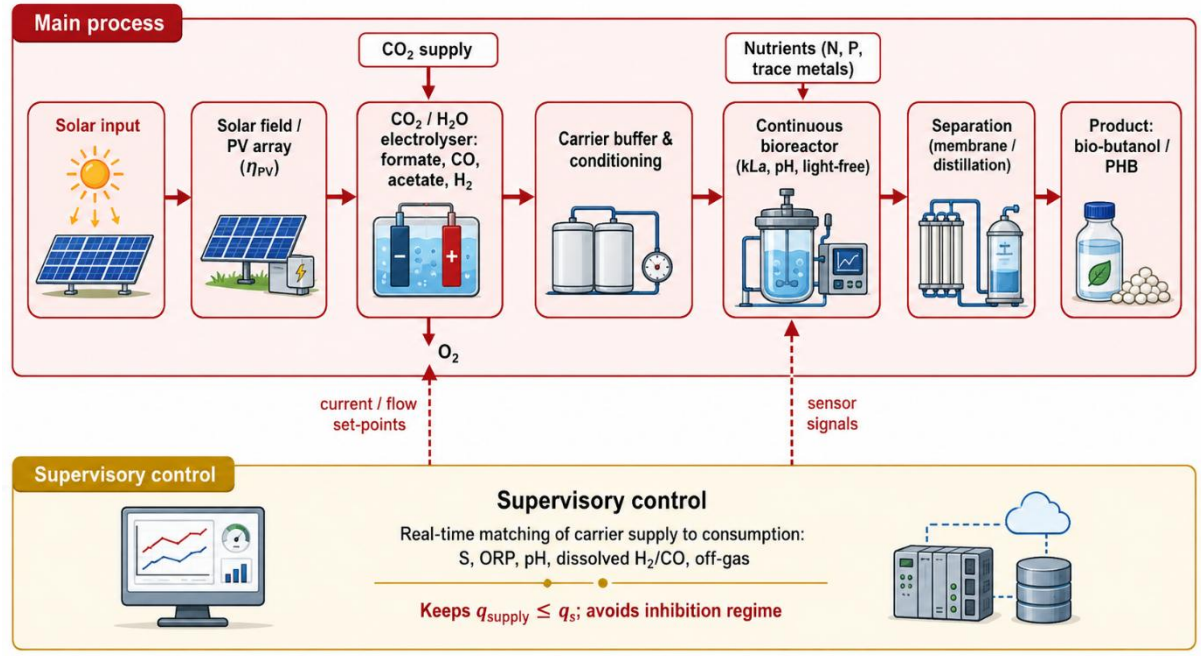


Figure 7. Process flow for Architecture A with supervisory control. A buffer between electrolyser and bioreactor decouples solar intermittency from continuous fermentation; sensor-based set-points keep carrier supply below uptake capacity.

7.2 Mass transfer, hydrodynamics and reactor sizing

Formate oxidation by *C. necator* is aerobic, so oxygen transfer limits productivity. For stirred, gassed vessels the volumetric mass-transfer coefficient is commonly estimated by the correlation of van 't Riet (1979),

$$k_L a = A \left(\frac{P_g}{V}\right)^{\alpha} v_g{}^{\beta} \tag{5}$$

with A = 0.026, α = 0.4 and β = 0.5 for coalescing air–water systems (k_La in s^{-1}, P_g/V in W m^{-3}, v_g in m s^{-1}); a different parameter set applies to electrolyte-containing, non-coalescing media, so the correlation should be treated as an estimate to be verified by gassing-out experiments (Garcia-Ochoa and Gomez, 2009). Table 5 lists the preliminary scale-up design basis. Using Eq. (5) in reverse, the stated k_La values imply superficial gas velocities of 0.023, 0.017 and 0.011 m s^{-1} at bench, pilot and industrial scale, respectively (Figure 8), whereas the gas-lift design in Section 7.2 assumes 0.08 m s^{-1}; at that velocity and 1.1 kW m^{-3} the correlation would give about 0.12 s^{-1}. The scale-up design basis therefore needs reconciliation by measurement before it is used for procurement.

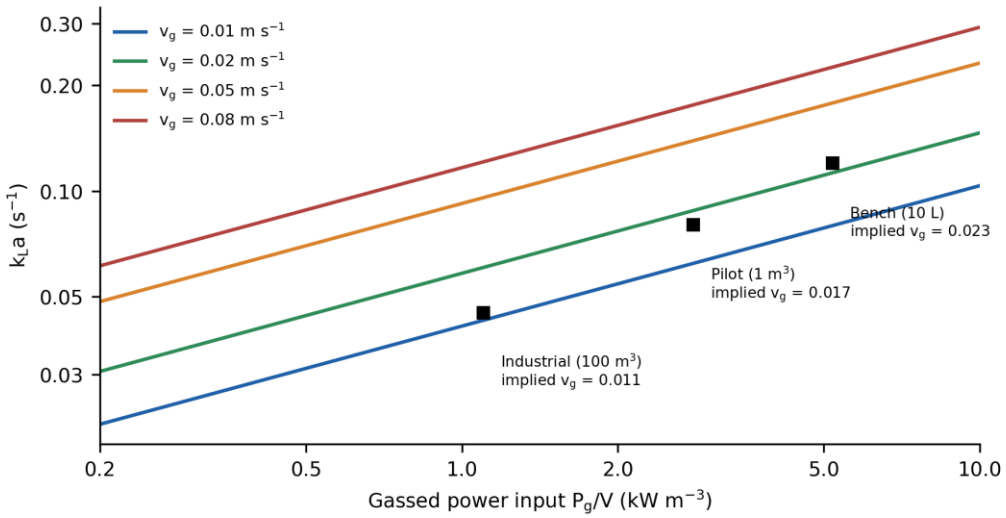


Figure 8. Estimated k_La from the van 't Riet correlation and the implied gas velocities of the design points. Curves: Eq. (5) for four superficial gas velocities. Squares: stated k_La at the stated P_g/V for each scale (Table 5).

Gas-lift (airlift) reactors are attractive at large scale because they provide gas–liquid contact, circulation and moderate shear without a mechanical impeller (Chisti and Moo-Young, 1987). The preliminary design uses a draft-tube gas-lift loop with three perforated trays at 3.75, 7.50 and 11.25 m, a 15 m column, a sparger ring and internal cooling coils in the downcomer. A geometry check is nevertheless required: a column of 2.10 m diameter and 15 m height holds only about 52.0 m^3, not the target 100 m^3 working volume, and has H/D = 7.14 rather than the 5.0 given in Table 5. Keeping H = 15 m and an area ratio $A_d/A_r = 1.5$, a 100 m^3 working volume requires D_{tank} = 2.91 m (H/D = 5.15), A_r = 2.67 m^2, A_d = 4.00 m^2 and D_{dt} = 1.84 m (Figure 9); alternatively, two parallel columns of the original diameter would be needed.

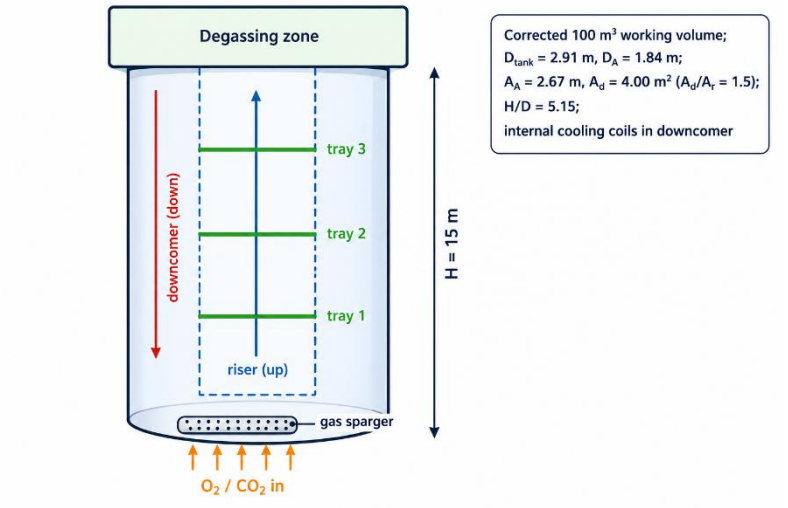


Figure 9. Corrected geometry of the 100 m^3 staged gas-lift reactors. The draft tube forms the riser; three perforated trays improve gas redistribution; the annular downcomer houses cooling coils.

To limit shear damage the maximum local stress should stay below a critical value, here taken as $\tau_{crit} \approx 15$ Pa for *C. necator*, with

$$\tau_{max} = \rho\sqrt{\nu\varepsilon_{max}} \tag{6}$$

where ρ is the liquid density, ν the kinematic viscosity and ε_{max} the maximum local energy-dissipation rate (W kg^{-1}). The dimensionally consistent form is $\rho(\nu\varepsilon_{max})^{1/2}$; for water-like broth ($\rho = 1000$ kg m^{-3}, $\nu = 10^{-6}$ m^2 s^{-1}) the limit of 15 Pa corresponds to $\varepsilon_{max} \approx 225$ W kg^{-1}. This is a design target requiring validation with the actual broth rheology.

Table 5. Preliminary scale-up design basis for the formate-fed *C. necator* bioreactor.

Parameter	Bench (10 L)	Pilot (1,000 L)	Industrial (100,000 L)
Reactor type	CSTR, mechanical agitation	Gas-lift loop / CSTR	Multi-stage gas-lift loop
Aspect ratio, H/D	2.1	3.5	5.0 (design target)
Agitation mode	Rushton turbine	Dual Rushton / hydrofoil	Micro-bubble sparged gas-lift
Gassed power, P_g/V (kW m^{-3})	5.2	2.8	1.1
k_La, stated (s^{-1})	0.12	0.08	0.045
Implied v_g from Eq. (5) (m s^{-1})	0.023	0.017	0.011
Target cell density, X (g L^{-1})	25	65	85
Volumetric yield (g PHB L^{-1} d^{-1})	12.4	38.2	52.0
Heat removal	Water jacket	External heat exchanger	Internal plate / coil exchangers

Rows 1–5 and 7–9 are the authors' design assumptions; the implied v_g row is computed from Eq. (5). Yields and cell densities are targets, not measurements.

7.3 Dynamic formate control

In a continuous stirred-tank reactor with cell retention (so that X is approximately constant) and equal inflow and outflow, the formate mass balance is

$$\frac{dS}{dt} = D\left(S_{feed} - S\right) - q_S(S)X \tag{7}$$

where $D = F_{in}/V$ is the dilution (feed) rate and S_{feed} the concentrated formate stream (5 M) from the electrolyser; $q_S(S)$ follows Eq. (2) with $K_S = 0.8$ mM and $K_I = 120$ mM. We assume $q_{max} = 25$ mmol g^{-1} h^{-1} and $X = 60$ g L^{-1}; these two values are illustrative assumptions rather than measured constants. The target window is 15–35 mM formate, centred on 25 mM, for which the nominal feed rate is $D^* = 0.243$ h^{-1}. Notably, the whole window lies above $S_{opt} = 9.8$ mM, on the descending branch of the uptake curve ($q_S = 20.2$ versus 21.5 mmol g^{-1} h^{-1} at the peak), so the operating point is open-loop unstable: linearisation gives a positive pole of 6.6 h^{-1}. A proportional gain must therefore exceed $K_{p,min} = 0.001$ h^{-1} mM^{-1} for closed-loop stability, which means that any scheme that lowers controller gain during rapid transients must keep the gain above this threshold. Operating nearer S_{opt} would remove the instability at a cost of only a few percent of uptake capacity.

We simulated 24 h of operation with a pump capacity of $D_{max} = 0.40$ h^{-1} and two disturbances: a 50% loss of uptake capacity between 10 and 14 h (for example an oxygen-limitation episode),

and a collapse of formate supply capacity to 0.08 h^{-1} between 18 and 19.5 h (a cloud transient without buffer storage). Three strategies were compared: constant nominal feed (open loop); a PI controller with feed-forward; and the same PI controller with back-calculation anti-windup (Åström and Rundqwist, 1989; Åström and Hägglund, 2006),

$$u = D_* + K_p e + I,\ \frac{dI}{dt} = K_i e + K_t(D - u),\ D = sat(u; 0, D_{max}) \tag{8}$$

with e = S_{sp} − S, K_p = 0.004 h^{-1} mM^{-1}, K_i = 0.03 h^{-2} mM^{-1} and K_t = 20 h^{-1}. Figure 10 and Table 6 summarise the results. In open loop, the 10-h disturbance pushes S over the unstable threshold, and it diverges towards the feed concentration (4.6 M after 24 h), spending only 0.1% of the time in the window. Both PI variants recover and return to the set-point, but when the feed saturates during the supply collapses the unprotected integrator winds up and, once supply is restored, drives S to 207 mM. Back-calculation anti-windup limits the peak to 48 mM and reduces the integrated absolute error from 99.8 to 56.1 mM h. Neither can controllers prevent carrier starvation (S falls to 0.29 mM) while supply capacity is below demand, which is why the buffer tank in Figure 7 is essential. The simulation is a screening demonstration with assumed kinetic parameters; implementation would require measured q_{max}(t), a validated sensor for S (or a pH/dissolved-oxygen surrogate), and tuning on the real process.

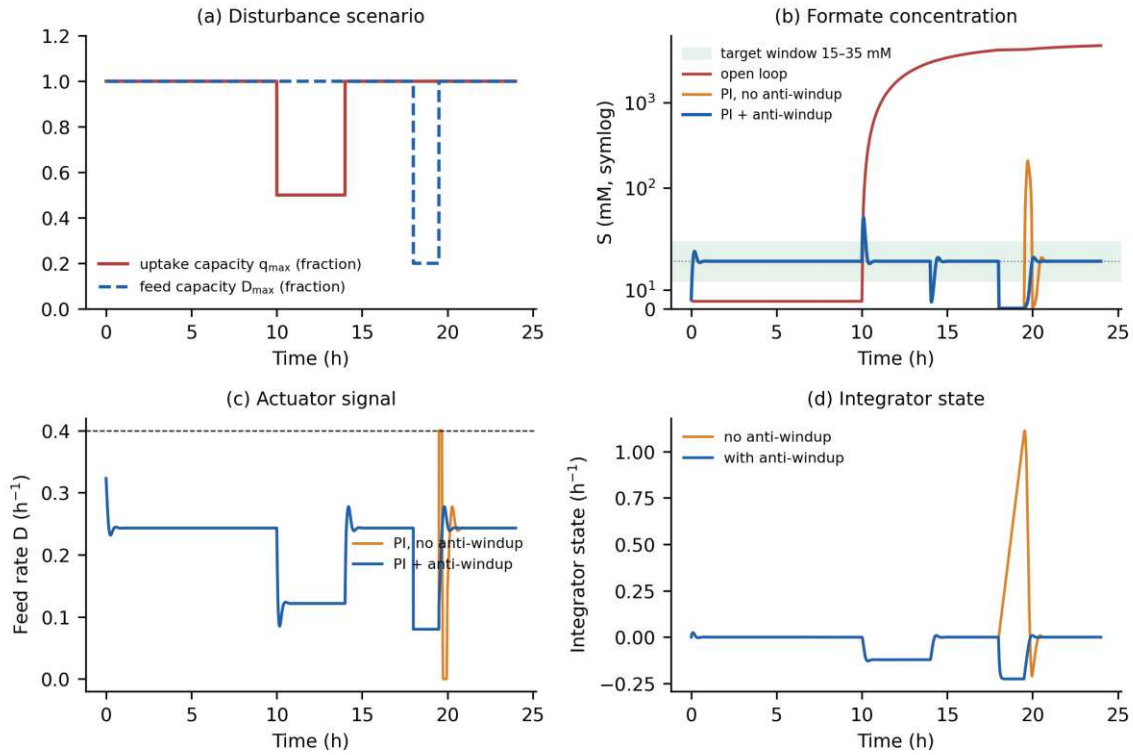


Figure 10. Simulated formate control under uptake and supply disturbances. (a) Disturbance scenario. (b) Formate concentration (symmetric-log axis; shaded band is the 15–35 mM window). (c) Feed-rate signal; the dashed line is the pump limit. (d) Integrator state, showing windup without back-calculation.

Table 6. Control performance over 24 h (simulation).

Strategy	Peak S (mM)	Time in 15–35 mM window (%)	IAE (mM h)	Minimum S (mM)
Open loop (nominal feed)	4603	0.1	diverges	3.96
PI, no anti-windup	207	88.7	99.8	0.29
PI + back-calculation anti-windup	48	90.4	56.1	0.29

IAE, integral of $|S_{sp} - S|$ over 24 h (S clipped at 200 mM for the integral). Initial S = 5 mM; the start-up transient and the supply collapse account for most of the time outside the window.

7.4 Downstream processing of PHB

Because intracellular PHB must be recovered from dense biomass, downstream processing (DSP) is a major contributor to cost and environmental burden (Jacquel et al., 2008). The preliminary DSP train comprises continuous disk-stack centrifugation to concentrate cells from 85 to 220 g L^{-1}, high-pressure homogenisation (800 bar, two passes), alkaline digestion of non-polymer cell material (pH 11.5, 40 °C) and green-solvent or supercritical-CO_2 extraction, with design targets of more than 98% polymer recovery at 99.2% purity. These are design targets rather than demonstrated performance, and the energy consumption of the train should be reported alongside purity and recovery in future work.

8. Techno-economic screening

We re-evaluated the authors' preliminary plant model for Pathway A (decoupled PV–EC–fermentation, PV-EC-F) and Pathway B (direct PEC–biohybrid, PEC-Bio) at 10,000 t PHB yr^{-1}, a 20-year life and an 8% discount rate. The levelised cost of product is computed with a capital recovery factor (CRF),

$$LCOP = \frac{CRF \cdot CAPEX + OPEX_{fix} + OPEX_{var}}{Q_P}, \; CRF = \frac{r(1+r)^N}{(1+r)^N - 1} \tag{9}$$

where $Q_P = 10^7$ kg yr^{-1}. With r = 8% and N = 20 years, CRF = 0.102. This is a levelised screening metric; a full discount-cash-flow rate-of-return analysis would add construction period, working capital, taxation and financing, none of which are specified in the preliminary model. Table 7 lists the techno-economic inputs of the preliminary model for both pathways and the recomputed levelised cost of product.

Table 7. Techno-economic inputs (authors' preliminary model) and recomputed levelised cost.

Item	Pathway A (PV-EC-F)	Pathway B (PEC-Bio)
Solar harvesting (US$ M)	24.5 (utility PV field)	Included in PEC modules
Electrolysers / PEC reactor arrays (US$ M)	18.2 (formate cells)	78.4 (immersed PEC photoreactors)
Fermentation and balance of plant (US$ M)	32.1	12.6
Downstream separation (US$ M)	14.8	16.2
Total CAPEX (US$ M)	89.6	107.2
Annualised capital at CRF = 0.102 (US$ M yr^{-1})	9.13	10.92
Fixed OPEX (US$ M yr^{-1})	4.2	7.1
Variable OPEX (US$ M yr^{-1})	8.6	14.3 (incl. electrode replacement)

Recomputed LCOP (US$ kg^{-1})	2.19	3.23

Other inputs: CO_2 US$40 t^{-1}; solar capacity factor 24%; 3.12 and 3.25 kg CO_2 per kg PHB for A and B. The levelised costs recomputed here are lower than the values US$2.85 and US$5.92 kg^{-1} stated in the original model, which cannot be reproduced from the listed inputs without additional financing and tax assumptions.

Two consistency checks are informative. First, the energy content of PHB (taken as 20 MJ kg^{-1}, 5.6 kWh kg^{-1}) times 10^7 kg yr^{-1} is 55.6 GWh yr^{-1}; the stated electricity demand of 18.4 kWh kg^{-1} (184 GWh yr^{-1}) therefore corresponds to an electricity-to-product efficiency of 30%, and with a 24%-efficient PV stage to $\eta_{STC} \approx 7.2\%$ rather than the 12% adopted in the original sensitivity analysis. Re-scaling the upstream (PV + electrolyser) cost with $1/\eta_{STC}$, Pathway A at 7.2% would cost US$2.48 kg^{-1}. Second, the stated CAPEX implies about 87.5 MW_p of PV at US$0.28 W_p^{-1} and an electrolyser cost near US$208 kW^{-1}; these unit costs are aggressive and should be confirmed with current vendor quotations, so the LCOP should be read as a lower-bound screening estimate.

Sensitivity analysis for Pathway A (Figure 11a) shows that the discount rate has the largest effect (US$2.00–2.48 kg^{-1} for 5–12%), followed by variable OPEX excluding CO_2; improving η_{STC} from 10% to 18% changes LCOP by only about US$0.23 kg^{-1} because the upstream stages are under half of CAPEX. For Pathway B, lifetime of the replaceable photoelectrode fraction matters strongly. Assuming that a fraction f of the PEC module cost is replaced every L year (f = 0.10 as base case; Figure 11b), LCOP rises from US$3.23 kg^{-1} for a 20-year life to about US$4.00 kg^{-1} at L = 1 year and US$6.44 kg^{-1} at L = 0.25 year. Under these inputs B remains above An even for very long lifetimes, so lifetime improvement alone cannot close the gap; capital cost must also fall. Broader analyses of CO_2 electrolysis reach similar conclusions on the primacy of electricity cost and capital intensity (Jouny et al., 2018; De Luna et al., 2019).

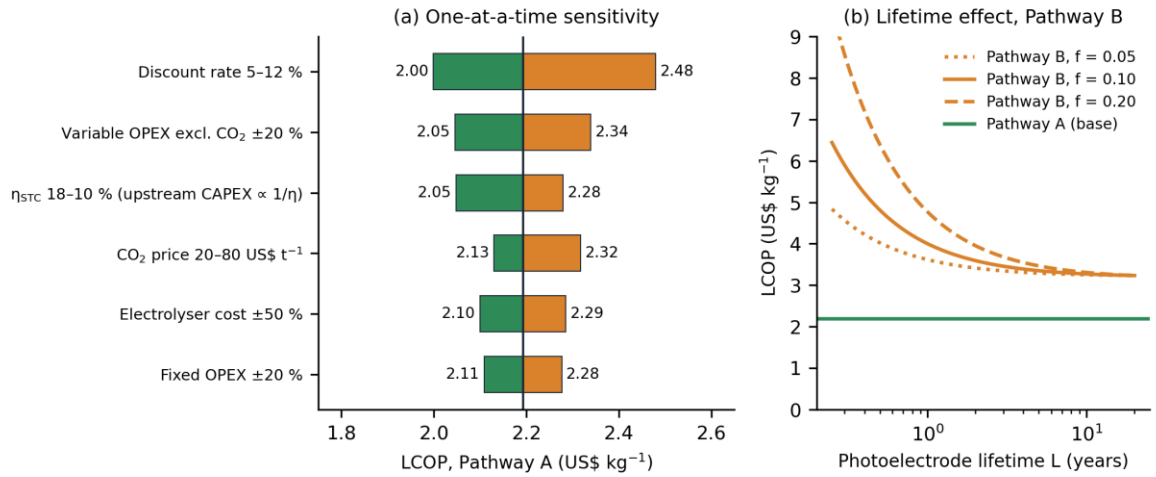


Figure 11. Sensitivity of the levelised cost of product (LCOP). (a) One-at-a-time sensitivity for Pathway A around the base value of US$2.19 kg^{-1}. (b) Effect of photoelectrode lifetime on Pathway B for replaceable fractions f of PEC module cost; the green line is Pathway A.

9. Life-cycle assessment

The functional unit is 1 kg of purified PHB at the plant gate, following the ISO 14040/14044 framework (ISO, 2006a; ISO, 2006b). The net global-warming potential (GWP) is

$$GWP_{net} = E_{emb} + E_{par} + E_{DSP} - C_{bio} \quad (10)$$

where the terms are embodied (capital, electrodes, infrastructure), parasitic-energy and downstream-processing emissions, and C_{bio} is the biogenic carbon contained in the product. PHB has the monomer formula $C_4H_6O_2$ (86.1 g mol^{-1}), so one kilogram contains carbon equivalent to $4M_{CO2}/M_{PHB}$ = 2.04 kg CO_2. This is the maximum biogenic credit that can be claimed per kilogram of polymer; the larger values of 3.12 and 3.25 kg CO_2 in the preliminary inventory represent gross CO_2 input, part of which is respired or leaves in co-products. Table 8 lists the inventory and results with consistent accounting; two corrections were made to the preliminary figures: the capital contribution of Pathway A was entered with a negative sign and is treated here as a burden (+0.2), and the downstream-processing burden (0.4) is applied to both pathways because both include downstream separation within the system boundary.

Table 8. Inventory and global warming potential (kg CO_2-eq per kg PHB).

Contribution	Pathway A (PV-EC-F)	Pathway B (PEC-Bio)	Polypropylene (benchmark)
Capital / electrode fabrication / infrastructure	+0.20	+2.70 (1.80 + 0.90)	–
Parasitic energy	+1.20	not separately stated	–
Downstream processing	+0.40	+0.40	–
Burden before biogenic credit	1.80	3.10	1.98
Biogenic carbon in product (credit)	−2.04	−2.04	–
Net GWP with credit	-0.24	1.06	1.98
Difference from benchmark: burden only	-9%	+57%	–
Difference from benchmark: with credit	-112%	-47%	–

Inventory entries are the authors' preliminary values; the benchmark of 1.98 kg CO_2-eq kg^{-1} is the value adopted in the original model and should be replaced with a cited database value. Mass balance (A/B): 3.12/3.25 kg CO_2, 18.4/42.1 kWh and 4.2/8.8 L H_2O per kg PHB, with 0.12/0.35 kg cell mass co-produced.

The results change the narrative. Before any biogenic credit, Pathway A has a burden of 1.80 kg CO_2-eq kg^{-1}, only about 9% below polypropylene, and Pathway B is higher than the fossil benchmark. A climate benefit appears mainly when the carbon stored in the polymer is credited (Figure 12), which is legitimate only if the carbon remains sequestered or if end-of-life emissions are accounted for symmetrically for both materials. Parasitic electricity is the largest burden in A and therefore depends directly on the carbon intensity of the supply; electrode fabrication dominates B. These findings parallel the land-use lessons from first-generation biofuels, where apparent savings disappeared once indirect emissions were counted (Fargione et al., 2008; Searchinger et al., 2008) and underline the importance of a boundary and allocation that are explicit and reproducible. Table 9 lists the remaining impact categories from the preliminary inventory; they point to higher water consumption for both pathways than for the

fossil benchmark and to metal-related toxicity and eutrophication risks for B, but they have not been independently validated.

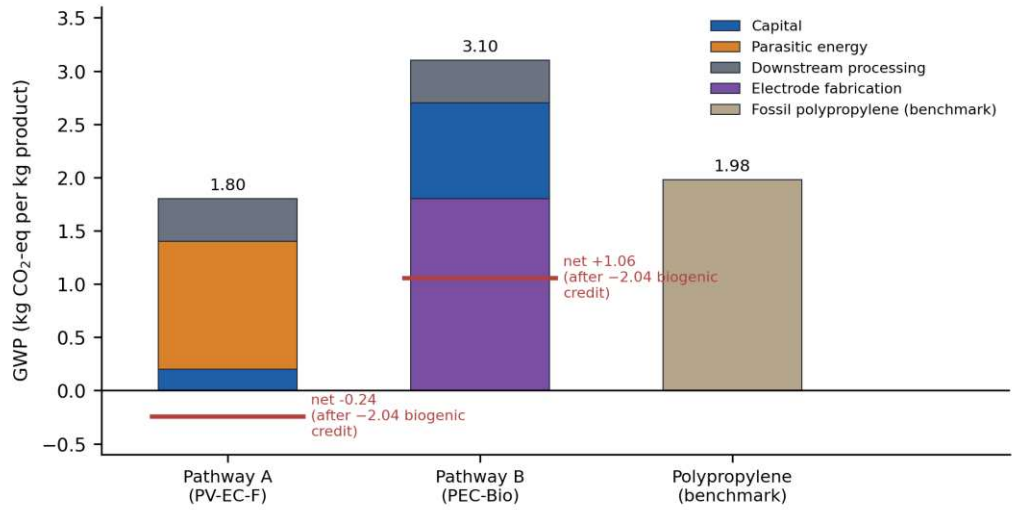


Figure 12. Global-warming potential of PHB pathways with consistent biogenic-carbon accounting. Stacked bars show burdens; red lines mark net GWP after the stoichiometric biogenic credit of 2.04 kg CO_2 per kg PHB.

Table 9. Additional impact categories per kg PHB (preliminary inventory values, not independently validated).

Impact category	Pathway A	Pathway B	Polypropylene
Eutrophication potential (g PO_4-eq)	0.42	1.85	0.85
Acidification potential (g SO_2-eq)	1.15	3.42	4.10
Human toxicity potential (kg 1,4-DCB-eq)	0.08	0.62	0.45
Water consumption (L)	12.5	28.4	4.2

10. Research roadmap and outlook

The analysis points to a small number of high-leverage priorities (Table 10). Reporting practice comes first: studies should state η_{STC} on an incident-sunlight and product-enthalpy basis, together with carbon balance, product titre and rate, and operating stability in hours, so that A, B and C can finally be compared on equal terms (Claassens et al., 2019; Fang et al., 2020). On the materials side, protective layers and biocompatible, possibly self-healing conductive interfaces are needed to extend photocathode life towards the multi-year region where economics become relevant (Hu et al., 2014; Chen and Wang, 2012). On the biological side, ROS tolerance through catalase and superoxide dismutase expression, capped or biogenic nanomaterials, and formate- or H_2-tolerant strains would raise K_I and widen the stable operating window (Imlay, 2013; Derfus et al., 2004; Gleizer et al., 2019). On the engineering side, closed-loop supply–demand control with anti-windup, buffer storage and measured k_La and shear limits are the near-term enablers of reliable scale-up (Åström and Hägglund, 2006; Garcia-Ochoa and Gomez, 2009; Chisti and Moo-Young, 1987). Finally, transparent inventories, uncertainty analysis and explicit end-of-life assumptions are needed for credible TEA and LCA (ISO, 2006a; ISO, 2006b).

Table 10. Prioritised research roadmap (proposed targets are the authors' recommendations).

Priority	Proposed target	Enabling approach	Key references
Standardised reporting	η_{STC} on incident-sunlight basis; full carbon and electron balance; operation ≥100 h	Common protocol; report quantum yield and η_{STC} separately	(Claassens et al., 2019; Fang et al., 2020)
Interface durability	Photoelectrode life ≥1 year in culture medium	Protective oxides; self-healing conductive polymers; antifouling	(Hu et al., 2014; Chen and Wang, 2012)
ROS and toxicity tolerance	Maintained activity under illumination without Cd release	Catalase/SOD expression; capped or biogenic absorbers	(Imlay, 2013; Derfus et al., 2004; Hossain and Mukherjee, 2013)
Carrier tolerance and redox balance	Higher K_I; wide stable window around S_{opt}	Strain engineering; flux analysis with redox constraints	(Gleizer et al., 2019; Orth et al., 2010; Nagarajan et al., 2013)
Control and buffering	Carrier supply ≤ uptake capacity under solar variability	Buffer tank; PI/MPC with anti-windup	(Åström and Rundqwist, 1989; Åström and Hägglund, 2006)
Reactor validation	Measured k_La and shear at pilot scale (≥1 m^3)	Gas-lift with staged trays; gassing-out tests	(Garcia-Ochoa and Gomez, 2009; Chisti and Moo-Young, 1987; van 't Riet, 1979)
Open TEA/LCA	Cited inventories, uncertainty ranges, end-of-life scenarios	ISO-compliant boundaries; Monte Carlo analysis	(ISO, 2006a; ISO, 2006b; Jouny et al., 2018)

11. Conclusions

Integrated artificial photosynthesis–microbial bioprocessing offers a credible route to converting sunlight and CO_2 into fuels and polymers at areal efficiencies several times those of crops, but its realisation depends on managing the interface between abiotic electron supply and biological demand. Architecture A currently has the strongest evidence base and the most favourable preliminary economics, B is constrained by photoelectrode lifetime and capital cost, and C by material toxicity and the difficulty of reporting solar-to-chemical efficiency. A cascade analysis bounds η_{STC} at 4.0–10.9% for A under explicit assumptions; substrate inhibition makes the carrier-supply problem a stability problem that closed-loop control with anti-windup can address in simulation; recomputed levelised costs are US$2.19 and US$3.23 kg^{-1} for A and B under the preliminary inputs; and life-cycle conclusions are sensitive to biogenic-carbon accounting. The numerical results from the plant, reactor and inventory model are screening estimates based on assumed inputs and should be replaced by measured data and vendor quotations as the work matures. Experimental priorities are long-lived interfaces, ROS- and carrier-tolerant strains, validated mass transfer and shear limits, and standardised reporting.

Declarations

Acknowledgment: Director ASET AUUP Lucknow Campus, Dr. Anil Kumar

Author contributions

Devesh Ojha: Conceptualization, Formal analysis, Methodology, Resources, Writing – original draft; **Bandana Ojha:** Methodology, Resources, Writing – original draft, review & editing.

Funding: Not Applicable

Conflicts of Interest/Competing Interests: The authors declare that they have no known competing financial interests or personal relationships that could have appeared to influence the work reported in this paper.

Ethical approval

Not applicable. This study is a literature review supplemented by computational screening calculations and did not involve human participants, human data, human tissue or animals.

Consent to participate

Not applicable. No human participants were involved in this study.

Consent to publish

Not applicable. The manuscript does not contain any individual person's data in any form.

Data availability statement: No new experimental datasets were generated in this study. All literature values are taken from the cited primary sources. The input assumptions, parameters and results of the screening calculations (efficiency cascade, kinetic and control simulations, techno-economic analysis and life-cycle inventory) are reported within the article.

References

Andrews, J. F. (1968). A mathematical model for the continuous culture of microorganisms utilizing inhibitory substrates. *Biotechnology and Bioengineering*, 10(6), 707–723. https://doi.org/10.1002/bit.260100602

Åström, K. J., & Rundqwist, L. (1989). Integrator windup and how to avoid it. In *Proceedings of the 1989 American Control Conference* (pp. 1693–1698). IEEE.

Åström, K. J., & Hägglund, T. (2006). *Advanced PID control*. ISA – The Instrumentation, Systems, and Automation Society, Research Triangle Park, NC.

Bar-Even, A., Noor, E., Lewis, N. E., & Milo, R. (2010). Design and analysis of synthetic carbon fixation pathways. *Proceedings of the National Academy of Sciences*, 107(19), 8889–8894. https://doi.org/10.1073/pnas.0907176107

Blankenship, R. E., Tiede, D. M., Barber, J., Brudvig, G. W., Fleming, G., Ghirardi, M., et al. (2011). Comparing photosynthetic and photovoltaic efficiencies and recognizing the potential for improvement. *Science*, 332(6031), 805–809. https://doi.org/10.1126/science.1200165

Cestellos-Blanco, S., Zhang, H., Kim, J. M., Shen, Y.-x., & Yang, P. (2020). Photosynthetic semiconductor biohybrids for solar-driven biocatalysis. *Nature Catalysis*, 3(3), 245–255. https://doi.org/10.1038/s41929-020-0428-y

Chen, S., & Wang, L.-W. (2012). Thermodynamic oxidation and reduction potentials of photocatalytic semiconductors in aqueous solution. *Chemistry of Materials*, 24(18), 3659–3666. https://doi.org/10.1021/cm302533s

Chen, H., Xia, A., Huang, Y., Ji, J., Zhang, J., Zhu, X., et al. (2026). Engineering a semi-artificial photosynthetic biofilm for robust and high-efficiency CO2-to-methane conversion. *Chemical Science*. Advance article. https://doi.org/10.1039/D6SC00459H

Cheng, W.-H., Richter, M. H., May, M. M., Ohlmann, J., Lackner, D., Dimroth, F., et al. (2018). Monolithic photoelectrochemical device for direct water splitting with 19% efficiency. *ACS Energy Letters*, 3(8), 1795–1800. https://doi.org/10.1021/acsenergylett.8b00920

Chisti, M. Y., & Moo-Young, M. (1987). Airlift reactors: Characteristics, applications and design considerations. *Chemical Engineering Communications*, 60(1–6), 195–242. https://doi.org/10.1080/00986448708911967

Claassens, N. J., Sánchez-Andrea, I., Sousa, D. Z., & Bar-Even, A. (2018). Towards sustainable feedstocks: A guide to electron donors for microbial carbon fixation. *Current Opinion in Biotechnology*, 50, 195–205. https://doi.org/10.1016/j.copbio.2018.01.019

Claassens, N. J., Cotton, C. A. R., Kopljar, D., & Bar-Even, A. (2019). Making quantitative sense of electromicrobial production. *Nature Catalysis*, 2(5), 437–447. https://doi.org/10.1038/s41929-019-0272-0

De Luna, P., Hahn, C., Higgins, D., Jaffer, S. A., Jaramillo, T. F., & Sargent, E. H. (2019). What would it take for renewably powered electrosynthesis to displace petrochemical processes?. *Science*, 364(6438), eaav3506. https://doi.org/10.1126/science.aav3506

Derfus, A. M., Chan, W. C. W., & Bhatia, S. N. (2004). Probing the cytotoxicity of semiconductor quantum dots. *Nano Letters*, 4(1), 11–18. https://doi.org/10.1021/nl0347334

Ding, Y., Bertram, J. R., Eckert, C., Bommareddy, R. R., Patel, R., Conradie, A., et al. (2019). Nanorg microbial factories: Light-driven renewable biochemical synthesis using quantum dot–bacteria nanobiohybrids. *Journal of the American Chemical Society*, 141(26), 10272–10282. https://doi.org/10.1021/jacs.9b02549

Dogutan, D. K., & Nocera, D. G. (2019). Artificial photosynthesis at efficiencies greatly exceeding that of natural photosynthesis. *Accounts of Chemical Research*, 52(11), 3143–3148. https://doi.org/10.1021/acs.accounts.9b00380

Fang, X., Kalathil, S., & Reisner, E. (2020). Semi-biological approaches to solar-to-chemical conversion. *Chemical Society Reviews*, 49(14), 4926–4952. https://doi.org/10.1039/C9CS00496C

Fargione, J., Hill, J., Tilman, D., Polasky, S., & Hawthorne, P. (2008). Land clearing and the biofuel carbon debt. *Science*, 319(5867), 1235–1238. https://doi.org/10.1126/science.1152747

Garcia-Ochoa, F., & Gomez, E. (2009). Bioreactor scale-up and oxygen transfer rate in microbial processes: An overview. *Biotechnology Advances*, 27(2), 153–176. https://doi.org/10.1016/j.biotechadv.2008.10.006

Gleizer, S., Ben-Nissan, R., Bar-On, Y. M., Antonovsky, N., Noor, E., Zohar, Y., et al. (2019). Conversion of Escherichia coli to generate all biomass carbon from CO2. *Cell*, 179(6), 1255–1263. https://doi.org/10.1016/j.cell.2019.11.009

Guo, J., Suástegui, M., Sakimoto, K. K., Moody, V. M., Xiao, G., Nocera, D. G., et al. (2018). Light-driven fine chemical production in yeast biohybrids. *Science*, 362(6416), 813–816. https://doi.org/10.1126/science.aat9777

Haas, T., Krause, R., Weber, R., Demler, M., & Schmid, G. (2018). Technical photosynthesis involving CO2 electrolysis and fermentation. *Nature Catalysis*, 1(1), 32–39. https://doi.org/10.1038/s41929-017-0005-1

Hann, E. C., Overa, S., Harland-Dunaway, M., Narvaez, A. F., Le, D. N., Orozco-Cárdenas, M. L., Jiao, F., & Jinkerson, R. E. (2022). A hybrid inorganic–biological artificial photosynthesis system for energy-efficient food production. *Nature Food*, 3(6), 461–471. https://doi.org/10.1038/s43016-022-00530-x

Hossain, S. T., & Mukherjee, S. K. (2013). Toxicity of cadmium sulfide (CdS) nanoparticles against Escherichia coli and HeLa cells. *Journal of Hazardous Materials*, 260, 1073–1082. https://doi.org/10.1016/j.jhazmat.2013.07.005

Hu, S., Shaner, M. R., Beardslee, J. A., Lichterman, M., Brunschwig, B. S., & Lewis, N. S. (2014). Amorphous TiO2 coatings stabilize Si, GaAs, and GaP photoanodes for efficient water oxidation. *Science*, 344(6187), 1005–1009. https://doi.org/10.1126/science.1251428

Imlay, J. A. (2008). Cellular defenses against superoxide and hydrogen peroxide. *Annual Review of Biochemistry*, 77, 755–776. https://doi.org/10.1146/annurev.biochem.77.061606.161055

Imlay, J. A. (2013). The molecular mechanisms and physiological consequences of oxidative stress: Lessons from a model bacterium. *Nature Reviews Microbiology*, 11(7), 443–454. https://doi.org/10.1038/nrmicro3032

ISO (2006a). *ISO 14040:2006 Environmental management — Life cycle assessment — Principles and framework*. International Organization for Standardization, Geneva.

ISO (2006b). *ISO 14044:2006 Environmental management — Life cycle assessment — Requirements and guidelines*. International Organization for Standardization, Geneva.

Jacquel, N., Lo, C.-W., Wei, Y.-H., Wu, H.-S., & Wang, S. S. (2008). Isolation and purification of bacterial poly(3-hydroxyalkanoates). *Biochemical Engineering Journal*, 39(1), 15–27. https://doi.org/10.1016/j.bej.2007.11.029

Jia, J., Seitz, L. C., Benck, J. D., Huo, Y., Chen, Y., Ng, J. W. D., et al. (2016). Solar water splitting by photovoltaic-electrolysis with a solar-to-hydrogen efficiency over 30%. *Nature Communications*, 7, 13237. https://doi.org/10.1038/ncomms13237

Jin, S., Jeon, Y., Jeon, M. S., Shin, J., Song, Y., Kang, S., et al. (2021). Acetogenic bacteria utilize light-driven electrons as an energy source for autotrophic growth. *Proceedings of the National Academy of Sciences*, 118(9), e2020552118. https://doi.org/10.1073/pnas.2020552118

Jouny, M., Luc, W., & Jiao, F. (2018). General techno-economic analysis of CO2 electrolysis systems. *Industrial & Engineering Chemistry Research*, 57(6), 2165–2177. https://doi.org/10.1021/acs.iecr.7b03514

Kim, D., Sakimoto, K. K., Hong, D., & Yang, P. (2015). Artificial photosynthesis for sustainable fuel and chemical production. *Angewandte Chemie International Edition*, 54(11), 3259–3266. https://doi.org/10.1002/anie.201409116

Kornienko, N., Sakimoto, K. K., Herlihy, D. M., Nguyen, S. C., Alivisatos, A. P., Harris, C. B., et al. (2016). Spectroscopic elucidation of energy transfer in hybrid inorganic–biological organisms for solar-to-chemical production. *Proceedings of the National Academy of Sciences*, 113(42), 11750–11755. https://doi.org/10.1073/pnas.1610554113

Kornienko, N., Zhang, J. Z., Sakimoto, K. K., Yang, P., & Reisner, E. (2018). Interfacing nature's catalytic machinery with synthetic materials for semi-artificial photosynthesis. *Nature Nanotechnology*, 13(10), 890–899. https://doi.org/10.1038/s41565-018-0251-7

Kracke, F., Vassilev, I., & Krömer, J. O. (2015). Microbial electron transport and energy conservation – the foundation for optimizing bioelectrochemical systems. *Frontiers in Microbiology*, 6, 575. https://doi.org/10.3389/fmicb.2015.00575

Lewis, N. S., & Nocera, D. G. (2006). Powering the planet: Chemical challenges in solar energy utilization. *Proceedings of the National Academy of Sciences*, 103(43), 15729–15735. https://doi.org/10.1073/pnas.0603395103

Li, H., Opgenorth, P. H., Wernick, D. G., Rogers, S., Wu, T.-Y., Higashide, W., et al. (2012). Integrated electromicrobial conversion of CO2 to higher alcohols. *Science*, 335(6076), 1596. https://doi.org/10.1126/science.1217643

Liew, F., Martin, M. E., Tappel, R. C., Heijstra, B. D., Mihalcea, C., & Köpke, M. (2016). Gas fermentation—A flexible platform for commercial scale production of low-carbon-fuels and chemicals from waste and renewable feedstocks. *Frontiers in Microbiology*, 7, 694. https://doi.org/10.3389/fmicb.2016.00694

Liu, C., Gallagher, J. J., Sakimoto, K. K., Nichols, E. M., Chang, C. J., Chang, M. C. Y., et al. (2015). Nanowire–bacteria hybrids for unassisted solar carbon dioxide fixation to value-added chemicals. *Nano Letters*, 15(5), 3634–3639. https://doi.org/10.1021/acs.nanolett.5b01254

Liu, C., Colón, B. C., Ziesack, M., Silver, P. A., & Nocera, D. G. (2016). Water splitting–biosynthetic system with CO2 reduction efficiencies exceeding photosynthesis. *Science*, 352(6290), 1210–1213. https://doi.org/10.1126/science.aaf5039

Logan, B. E., Rossi, R., Ragab, A., & Saikaly, P. E. (2019). Electroactive microorganisms in bioelectrochemical systems. *Nature Reviews Microbiology*, 17(5), 307–319. https://doi.org/10.1038/s41579-019-0173-x

Lovley, D. R. (2017). Syntrophy goes electric: Direct interspecies electron transfer. *Annual Review of Microbiology*, 71, 643–664. https://doi.org/10.1146/annurev-micro-030117-020420

Monk, J. M., Lloyd, C. J., Brunk, E., Mih, N., Sastry, A., King, Z., et al. (2017). iML1515, a knowledgebase that computes Escherichia coli traits. *Nature Biotechnology*, 35(10), 904–908. https://doi.org/10.1038/nbt.3956

Nagarajan, H., Sahin, M., Nogales, J., Latif, H., Lovley, D. R., Ebrahim, A., et al. (2013). Characterizing acetogenic metabolism using a genome-scale metabolic reconstruction of Clostridium ljungdahlii. *Microbial Cell Factories*, 12, 118. https://doi.org/10.1186/1475-2859-12-118

Nevin, K. P., Woodard, T. L., Franks, A. E., Summers, Z. M., & Lovley, D. R. (2010). Microbial electrosynthesis: Feeding microbes electricity to convert carbon dioxide and water to multicarbon extracellular organic compounds. *mBio*, 1(2), e00103-10. https://doi.org/10.1128/mBio.00103-10

Nichols, E. M., Gallagher, J. J., Liu, C., Su, Y., Resasco, J., Yu, Y., et al. (2015). Hybrid bioinorganic approach to solar-to-chemical conversion. *Proceedings of the National Academy of Sciences*, 112(37), 11461–11466. https://doi.org/10.1073/pnas.1508075112

Novak, M., Marđetko, N., Trontel, A., Pavlečić, M., Kelemen, Z., Perković, L., Petravić Tominac, V., & Šantek, B. (2024). Development of an integrated bioprocess system for bioethanol and arabitol production from sugar beet cossettes. *Food Technology and Biotechnology*, 62(1), 89–101. https://doi.org/10.17113/ftb.62.01.24.8230

Orth, J. D., Thiele, I., & Palsson, B. Ø. (2010). What is flux balance analysis?. *Nature Biotechnology*, 28(3), 245–248. https://doi.org/10.1038/nbt.1614

Pagliano, G., Ventorino, V., Panico, A., & Pepe, O. (2017). Integrated systems for biopolymers and bioenergy production from organic waste and by-products: A review of microbial processes. *Biotechnology for Biofuels*, 10, 113. https://doi.org/10.1186/s13068-017-0802-4

Prévoteau, A., Carvajal-Arroyo, J. M., Ganigué, R., & Rabaey, K. (2020). Microbial electrosynthesis from CO2: Forever a promise?. *Current Opinion in Biotechnology*, 62, 48–57. https://doi.org/10.1016/j.copbio.2019.08.014

Rabaey, K., & Rozendal, R. A. (2010). Microbial electrosynthesis — revisiting the electrical route for microbial production. *Nature Reviews Microbiology*, 8(10), 706–716. https://doi.org/10.1038/nrmicro2422

Ragsdale, S. W., & Pierce, E. (2008). Acetogenesis and the Wood–Ljungdahl pathway of CO2 fixation. *Biochimica et Biophysica Acta – Proteins and Proteomics*, 1784(12), 1873–1898. https://doi.org/10.1016/j.bbapap.2008.08.012

Reinecke, F., & Steinbüchel, A. (2009). Ralstonia eutropha strain H16 as model organism for PHA metabolism and for biotechnological production of technically interesting biopolymers. *Journal of Molecular Microbiology and Biotechnology*, 16(1–2), 91–108. https://doi.org/10.1159/000142897

van 't Riet, K. (1979). Review of measuring methods and results in nonviscous gas-liquid mass transfer in stirred vessels. *Industrial & Engineering Chemistry Process Design and Development*, 18(3), 357–364. https://doi.org/10.1021/i260071a001

Rishan, M., Punathil, P., Burns, C., Arca, E., do Nascimento, J., Lazarov, V. K., et al. (2026). Cu2ZnSnS4–Sporomusa ovata photobiohybrids coupled with Clostridium kluyveri fermentation for CO2 conversion to C4–C6 fatty acids. *Materials Horizons*. Advance article. https://doi.org/10.1039/d5mh02330k

Sakimoto, K. K., Wong, A. B., & Yang, P. (2016). Self-photosensitization of nonphotosynthetic bacteria for solar-to-chemical production. *Science*, 351(6268), 74–77. https://doi.org/10.1126/science.aad3317

Sakimoto, K. K., Kornienko, N., Cestellos-Blanco, S., Lim, J., Liu, C., & Yang, P. (2018). Physical biology of the materials–microorganism interface. *Journal of the American Chemical Society*, 140(6), 1978–1985. https://doi.org/10.1021/jacs.7b11135

Schuchmann, K., & Müller, V. (2014). Autotrophy at the thermodynamic limit of life: A model for energy conservation in acetogenic bacteria. *Nature Reviews Microbiology*, 12(12), 809–821. https://doi.org/10.1038/nrmicro3365

Schwander, T., Schada von Borzyskowski, L., Burgener, S., Cortina, N. S., & Erb, T. J. (2016). A synthetic pathway for the fixation of carbon dioxide in vitro. *Science*, 354(6314), 900–904. https://doi.org/10.1126/science.aah5237

Searchinger, T., Heimlich, R., Houghton, R. A., Dong, F., Elobeid, A., Fabiosa, J., et al. (2008). Use of U.S. croplands for biofuels increases greenhouse gases through emissions from land-use change. *Science*, 319(5867), 1238–1240. https://doi.org/10.1126/science.1151861

Shi, L., Dong, H., Reguera, G., Beyenal, H., Lu, A., Liu, J., et al. (2016). Extracellular electron transfer mechanisms between microorganisms and minerals. *Nature Reviews Microbiology*, 14(10), 651–662. https://doi.org/10.1038/nrmicro.2016.93

Stephens, S., Mahadevan, R., & Allen, D. G. (2021). Engineering photosynthetic bioprocesses for sustainable chemical production: A review. *Frontiers in Bioengineering and Biotechnology*, 8, 610723. https://doi.org/10.3389/fbioe.2020.610723

Su, Y., Cestellos-Blanco, S., Kim, J. M., Shen, Y.-x., Kong, Q., Lu, D., et al. (2020). Close-packed nanowire-bacteria hybrids for efficient solar-driven CO2 fixation. *Joule*, 4(4), 800–811. https://doi.org/10.1016/j.joule.2020.03.001

Torella, J. P., Gagliardi, C. J., Chen, J. S., Bediako, D. K., Colón, B., Way, J. C., et al. (2015). Efficient solar-to-fuels production from a hybrid microbial–water-splitting catalyst system. *Proceedings of the National Academy of Sciences*, 112(8), 2337–2342. https://doi.org/10.1073/pnas.1424872112

Wang, B., Zeng, C., Chu, K. H., Wu, D., Yip, H. Y., Ye, L., et al. (2017). Enhanced biological hydrogen production from Escherichia coli with surface precipitated cadmium sulfide nanoparticles. *Advanced Energy Materials*, 7(20), 1700611. https://doi.org/10.1002/aenm.201700611

Yishai, O., Lindner, S. N., Gonzalez de la Cruz, J., Tenenboim, H., & Bar-Even, A. (2016). The formate bio-economy. *Current Opinion in Chemical Biology*, 35, 1–9. https://doi.org/10.1016/j.cbpa.2016.07.005

Zhang, H., Liu, H., Tian, Z., Lu, D., Yu, Y., Cestellos-Blanco, S., et al. (2018). Bacteria photosensitized by intracellular gold nanoclusters for solar fuel production. *Nature Nanotechnology*, 13(10), 900–905. https://doi.org/10.1038/s41565-018-0267-z

Zheng, T., Zhang, M., Wu, L., Guo, S., Liu, X., Zhao, J., et al. (2022). Upcycling CO2 into energy-rich long-chain compounds via electrochemical and metabolic engineering. *Nature Catalysis*, 5(5), 388–396. https://doi.org/10.1038/s41929-022-00775-6

Zhu, X.-G., Long, S. P., & Ort, D. R. (2008). What is the maximum efficiency with which photosynthesis can convert solar energy into biomass?. *Current Opinion in Biotechnology*, 19(2), 153–159. https://doi.org/10.1016/j.copbio.2008.02.004

Zhu, X.-G., Long, S. P., & Ort, D. R. (2010). Improving photosynthetic efficiency for greater yield. *Annual Review of Plant Biology*, 61, 235–261. https://doi.org/10.1146/annurev-arplant-042809-112206